

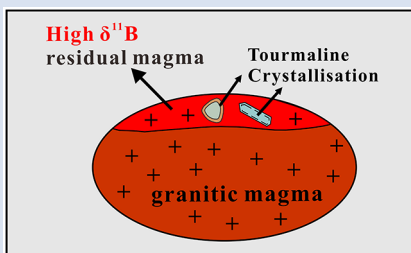
## Experiments reveal enrichment of $^{11}\text{B}$ in granitic melt resulting from tourmaline crystallisation

L. Cheng<sup>1,2\*</sup>, C. Zhang<sup>2,3\*</sup>, Y. Zhou<sup>1</sup>, I. Horn<sup>2</sup>, S. Weyer<sup>2</sup>, F. Holtz<sup>2</sup>



<https://doi.org/10.7185/geochemlet.2206>

### Abstract



Tourmaline is the most common boron-rich mineral in magmatic systems. In this study, we determined experimentally the fractionation of boron isotopes between granitic melt and tourmaline for the first time. Our crystallisation experiments were performed using a boron-rich granitic glass ( $\text{B}_2\text{O}_3 \approx 8$  wt. %) at 660–800 °C, 300 MPa, and  $a_{\text{H}_2\text{O}} = 1$ , in which tourmaline occurs as the only boron-hosting mineral. Our experimental results at four different temperatures show a small and temperature-dependent boron isotope fractionation between granitic melt and tourmaline ( $\Delta^{11}\text{B}_{\text{melt-Tur}} = +0.90 \pm 0.05$  ‰ at 660 °C and  $+0.23 \pm 0.12$  ‰ at 800 °C), and the temperature dependence can be defined as  $\Delta^{11}\text{B}_{\text{melt-Tur}} = 4.51 \times (1000/T [\text{K}]) - 3.94$  ( $R^2 = 0.96$ ). Using these boron isotope fractionation factors, tourmaline can serve

as a tracer to quantitatively interpret boron isotopic ratios in evolved magmatic systems. Our observation that  $^{11}\text{B}$  is enriched in granitic melt relative to tourmaline suggests that the  $\delta^{11}\text{B}$  of late-magmatic tourmaline should be higher than tourmaline that crystallised at an early stage, if B isotope fractionation is not affected by other processes, such as fluid loss.

Received 27 August 2021 | Accepted 25 January 2022 | Published 24 February 2022

### Introduction

Boron is an incompatible trace element that can be highly enriched in granitic melts and aqueous fluids (London *et al.*, 1996). The large difference in atomic mass by 10 % between the two stable isotopes of boron,  $^{10}\text{B}$  and  $^{11}\text{B}$ , results in significant variations in  $\delta^{11}\text{B}$  of natural rocks that can be up to ca. 100 ‰. The separation of B-rich phases such as tourmaline and aqueous fluid from silicate melt is expected to produce B isotope fractionation due to the different B coordination ( $^{11}\text{B}$  at trigonal site and  $^{10}\text{B}$  at tetrahedral site) in coexisting B-bearing phases (e.g., Trumbull *et al.*, 2013; Siegel *et al.*, 2016). Thus, B isotopes are a sensitive tool to trace magmatic–hydrothermal processes (such as fractional crystallisation, degassing, ore formation) and metamorphic fluid source, and tourmaline, as the most common B-hosting mineral in granitic magma, can serve as a useful tracer for such processes. The negligible intra-crystalline diffusion rate leads to the consequence that B isotopic composition of tourmaline is not easily overprinted by late magmatic or hydrothermal events and therefore ideal to record the evolution history of magmas (e.g., Marschall and Jiang, 2011). B isotope fractionation factors ( $\Delta^{11}\text{B}_{\text{melt-Tur}}$ ) between silicate melt and tourmaline are a prerequisite to quantitatively interpret the B isotope composition of tourmaline in granitic systems. To our knowledge, so far, B isotope fractionation between granitic melt and tourmaline has not been directly determined by experiments. In previous studies (e.g., Trumbull *et al.*, 2013; Siegel *et al.*, 2016),  $\Delta^{11}\text{B}_{\text{melt-Tur}}$  values were indirectly calculated from the combination of experimental results on B isotope fractionation between hydrous

melt and aqueous fluid ( $\Delta^{11}\text{B}_{\text{melt-fluid}}$ ) (Hervig *et al.*, 2002; Maner and London, 2018) and between tourmaline and aqueous fluid ( $\Delta^{11}\text{B}_{\text{Tur-fluid}}$ ) (Palmer *et al.*, 1992; Meyer *et al.*, 2008). However, these experimental studies differ in the experimental and analytical methods, the  $P$ - $T$  conditions, and the fluid compositions. Such discrepancies can lead to great uncertainties if these experimental results are used to calculate  $\Delta^{11}\text{B}_{\text{melt-Tur}}$  values. In addition, theoretical studies have suggested that the magnitude of  $\Delta^{11}\text{B}_{\text{Tur-fluid}}$  depends on the composition of tourmaline, with a larger fractionation for dravite than for schorl (Li *et al.*, 2020), which further increases the uncertainty for indirectly calculated  $\Delta^{11}\text{B}_{\text{melt-Tur}}$  values.

In this paper, we report results of tourmaline crystallisation experiments conducted for B-rich granitic systems in the temperature range of 660 to 800 °C and at 300 MPa. The analytical data of the B isotopic distribution between the experimental glasses and tourmalines provide direct constraints on the B isotope fractionation between granitic melt and tourmaline at magmatic temperatures.

### Methods

Five tourmaline crystallisation experiments were performed at 660–800 °C, 300 MPa,  $f_{\text{O}_2} \approx \text{NNO}$  for ~15–30 days in water-pressurised, cold-seal pressure vessels. A B-rich peraluminous granitic glass (B10 glass,  $\text{B}_2\text{O}_3 \approx 8.8$  wt. %), which was synthesised by melting mixed powders of a B-free glass (BDG-1) and

1. State Key Laboratory of Earthquake Dynamics, Institute of Geology, China Earthquake Administration, 100029 Beijing, China  
2. Institute of Mineralogy, Leibniz University Hannover, 30167, Hannover, Germany  
3. State Key Laboratory of Continental Dynamics, Department of Geology, Northwest University, 710069 Xi'an, China

\* Corresponding author (email: [chengling@ies.ac.cn](mailto:chengling@ies.ac.cn); [zhangchao@nwu.edu.cn](mailto:zhangchao@nwu.edu.cn))



boric acid powder, was used as starting material. Four water-saturated experiments ( $a_{\text{H}_2\text{O}} = 1$ ) and one water-undersaturated experiment ( $a_{\text{H}_2\text{O}} \approx 0.7$ ) were conducted. The activity of water was decreased by adding a fluid composed of mixed  $\text{H}_2\text{O}$  and  $\text{CO}_2$  (added as silver oxalate). Major element compositions of the starting glass and experimental products were measured by electron microprobe analyser (EMPA) using a Cameca SX-100 microprobe. Boron isotope compositions of the starting glass and experimental products were measured in situ using a Thermo Scientific Neptune Plus, which was connected to a Spectra-Physics Solstice femtosecond laser ablation system. Details on the experimental and analytical methods are reported in [Supplementary Information \(SI\)](#).

## Results

Experimental conditions and products are listed in [Table 1](#). Tourmaline was observed in all experiments and homogeneously distributed in melts as dark-green euhedral and columnar crystals, with a common size of  $\sim 100 \mu\text{m}$  in length and  $\sim 50 \mu\text{m}$  in width ([Fig. 1](#)). In back-scattered electron (BSE) images, most tourmalines show a variation in darkness even within one crystal ([Fig. 1b](#)), and some grains are characterised by faceted hourglass sector zoning (see details in [SI](#)) ([Fig. 1e, f](#)). The  $\text{Mg}/[\text{Mg} + \text{Fe}]$  ratio is *ca.* 0.35–0.55 ([Fig. S-2](#)), which is typical for schorl and consistent with that of common igneous tourmalines in nature. Minor amounts of magnetite are evenly distributed in experiments. Bubbles were found in runs DC-28 and DC-87. Experimental melts (quenched as glasses) are per-aluminous ( $\text{ASI} \approx 1.1\text{--}1.4$ ) and show a narrow range in  $\text{B}_2\text{O}_3$  content ( $\sim 7.7\text{--}8.0 \text{ wt. } \%$ ). Additional details about experimental products and phase compositions are given in [SI](#).

Boron isotopic compositions of the experimental tourmalines and glasses, as well as the calculated isotopic fractionation factors between them, are listed in [Table 1](#). The starting glass (B10) shows a homogeneous B isotope composition within error, with  $\delta^{11}\text{B}$  values of  $+0.92 \pm 0.03 \text{ ‰}$  ([Table S-5](#)). The B isotope composition of experimental glasses ( $\delta^{11}\text{B}_{\text{melt}}$ ) is close to that of the starting glass but displays a positive trend with temperature, increasing from  $+0.78 \pm 0.04 \text{ ‰}$  at  $660 \text{ °C}$  to  $+1.10 \pm 0.07 \text{ ‰}$  at  $800 \text{ °C}$  ([Table 1](#)). The low  $\delta^{11}\text{B}$  value of DC-87 glass relative to starting glass may result from the occurrence of a fluid phase in this experiment because  $^{11}\text{B}$  is expected to be preferentially

partitioned into fluid relative to granitic melt ([Maner and London, 2018](#)). The B isotopic compositions of the experimental tourmaline ( $\delta^{11}\text{B}_{\text{Tur}}$ ) show a positive correlation with temperature, increasing from  $-0.11 \pm 0.04 \text{ ‰}$  at  $660 \text{ °C}$  to  $+0.86 \pm 0.10 \text{ ‰}$  at  $800 \text{ °C}$  ([Table 1](#)). The calculated B isotope fractionation factors between melt and tourmaline ( $\Delta^{11}\text{B}_{\text{melt-Tur}}$ ) increase from  $+0.23 \pm 0.12 \text{ ‰}$  at  $800 \text{ °C}$  to  $+0.90 \pm 0.05 \text{ ‰}$  at  $660 \text{ °C}$  ([Table 1](#)), and data regression indicates that the temperature dependence on  $\Delta^{11}\text{B}_{\text{melt-Tur}}$  can be described as  $\Delta^{11}\text{B}_{\text{melt-Tur}} = 4.51 \times (1000/T [\text{K}]) - 3.94$  ( $R^2 = 0.96$ ) ([Fig. 2a](#)). In addition, the two experiments performed at  $800 \text{ °C}$  with different water activities (DC-27 and DC-28) show identical  $\Delta^{11}\text{B}_{\text{melt-Tur}}$  values within uncertainties.

## Discussion

Several lines of evidence suggest that near equilibrium conditions in terms of both major elements and B isotopes were reached between melt and tourmaline in our experiments: (1) microscopic observation shows that tourmaline is evenly distributed within the glass matrix for all experiments ([Fig. 1a](#)); (2) the major element compositions (seven to ten analytical points for each run) and B isotopic compositions (more than five analytical points) of experimental glasses from each experiment collected at different locations are identical within error ([Tables S-2 and S-6](#)); (3) apart from the hourglass sector zoning, no compositional zoning is observed in tourmaline; (4) no variation in B isotope composition is observed in experimental glasses next to the contact with tourmaline and far from the crystals (two or three points).

Our experimental data reveal a small and temperature-dependent B isotopic fractionation between granitic melt and tourmaline at magmatic temperatures. The degree of B isotopic fractionation between different phases at given  $P$ - $T$  conditions is considered to be mainly controlled by the coordination of B in each phase, with trigonal site favouring  $^{11}\text{B}$  and tetrahedral site favouring  $^{10}\text{B}$  ([Kowalski and Wunder, 2018](#)). B in tourmaline is almost exclusively coordinated at the trigonal site ( $^{11}\text{B}$ );  $^{10}\text{B}$  is expected in very Al-rich tourmaline ( $>1.2$  atoms Al per formula unit at the Y site) and at high pressures ( $>1000 \text{ MPa}$ ) and low temperatures ([Ertl \*et al.\*, 2018](#)). Our experimental tourmaline is thus assumed to contain negligible amounts of tetrahedrally coordinated B. However, the  $\delta^{11}\text{B}_{\text{Tur}}$  values show a systematic

**Table 1** Experimental conditions and boron isotopic fractionation factors and partition coefficients.

Run <sup>a</sup>	$\text{B}_2\text{O}_3$ content (wt. %) <sup>b</sup>	$T$ (°C)	$P$ (kbar)	$a_{\text{H}_2\text{O}}$ <sup>c</sup>	Duration (days)	Phases <sup>d</sup>	$\text{ASI}^e$	$\Delta^{11}\text{B}_{\text{melt}}$ (‰)	s.d. (‰)	$n$	$\Delta^{11}\text{B}_{\text{Tur}}$ (‰)	s.d. (‰)	$n$	$\Delta^{11}\text{B}_{\text{melt-Tur}}$ (‰)	s.d. (‰)	$\alpha$	$1000\ln\alpha$
DC-27	7.8	800	3	1.0	15	Tur (6.7), oxi (tr)	1.37	+1.10	0.07	5	+0.86	0.10	4	+0.23	0.12	1.0002	0.2308
DC-28	8.0	800	3	0.7	15	Tur (7.4), oxi (tr), fl	1.23	+1.10	0.02	5	+0.85	0.08	5	+0.25	0.09	1.0003	0.2559
DC-10	8.0	750	3	1.0	20	Tur (9), oxi (tr)	1.10	+0.96	0.08	6	+0.42	0.11	4	+0.54	0.13	1.0005	0.5459
DC-11	7.8	700	3	1.0	25	Tur (8.8)	1.20	+0.93	0.03	5	+0.31	0.11	4	+0.62	0.12	1.0006	0.6283
DC-87	7.7	660	3	1.0	30	Tur (10.8), oxi (tr), fl	1.24	+0.78	0.04	7	-0.11	0.04	4	+0.90	0.05	1.0009	0.9077

<sup>a</sup> Starting glass of all experiments was B10 glass.

<sup>b</sup> Boron contents of experimental glasses were measured by EMPA and calibrated based on data for synthesised glasses with different boron contents (B4, B6, and B10).

<sup>c</sup> Initial water activity in the experimental runs;  $a_{\text{H}_2\text{O}} = \text{H}_2\text{O}/(\text{H}_2\text{O} + \text{CO}_2)$  on a molar basis.

<sup>d</sup> Numbers in parentheses represent phase abundances in wt. %, which were calculated by mass balance; tr, trace amount, but abundance not determined. Phase abbreviations: Tur, tourmaline; oxi, oxide; fl, fluid.

<sup>e</sup> Aluminum saturation index in the experimental glass;  $\text{ASI} = \text{Al}_2\text{O}_3/(\text{Na}_2\text{O} + \text{K}_2\text{O} + \text{CaO})$  on a molar basis.



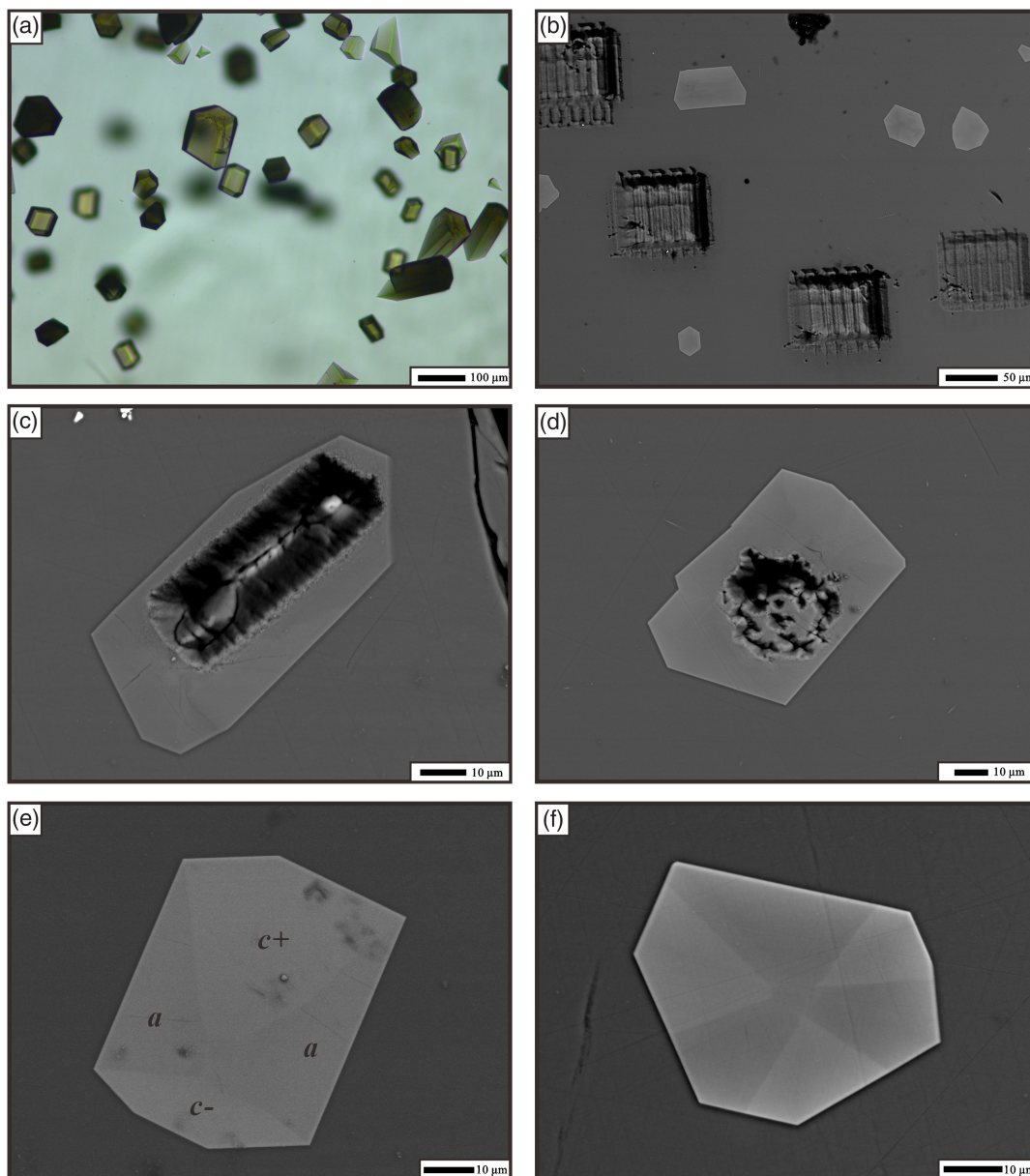


**Figure 1** Representative images of experimental products. **(a)** Tourmaline is evenly distributed in melts (run DC-11, plane-polarised). **(b, c, d)** Representative BSE images of runs DC-10, DC-28, and DC-11, respectively, showing the positions of analysed areas with laser-ablation. **(e)** BSE image of a tourmaline grain with hourglass sector zoning from DC-87, section nearly parallel to the *c*-axis. Three zones can be recognised in this crystal: *c*+, *c*−, and *a* sectors (see details in SI). **(f)** BSE image of a tourmaline grain from DC-11 with hourglass sector zoning, section perpendicular to the *c*-axis. The image shows faceted compositional sector zoning splitting the crystal into light and dark areas.

increase with increasing temperature, which could be interpreted as a positive temperature effect on stabilising  $^{14}\text{B}$  at the T-site of tourmaline (Ertl *et al.*, 2018). In hydrous silicate glasses, B occupies both trigonally and tetrahedrally coordinated sites, and the proportions of  $^{13}\text{B}$  and  $^{14}\text{B}$  depend on melt composition (especially on B content), temperature, and pressure (Dingwell *et al.*, 1996). Previous spectroscopic measurements indicate that the amount of  $^{14}\text{B}$  in both natural and synthetic glasses is minor and probably negligible (Tonarini *et al.*, 2003). Since most B in magmatic tourmaline is at trigonal sites, the small  $\Delta^{11}\text{B}_{\text{melt-Tur}}$  value implies that B should be predominantly at 3-fold coordinated sites in the peraluminous B-rich granitic melts of this study. The slight increase in  $\delta^{11}\text{B}_{\text{melt}}$  with increasing temperature in our experiments may be interpreted as the effect of temperature promoting the reaction  $[\text{BO}_4] \rightarrow [\text{BO}_3] + \text{NBO}$  in silicate

melts (Wu and Stebbins, 2013). It is noteworthy that some previous experimental studies observed a large B isotope fractionation between granitic melt and aqueous fluid, and interpreted it as an indication of a large proportion of  $^{14}\text{B}$  in the melt (Hervig *et al.*, 2002; Maner and London, 2018). This interpretation is inconsistent with both the result of this study and the spectroscopic studies.

This study provides a direct constraint on the B isotope fractionation between silicate melt and tourmaline and indicates a slightly positive value of  $\Delta^{11}\text{B}_{\text{melt-Tur}}$ . The  $\Delta^{11}\text{B}_{\text{melt-Tur}}$  estimated from fluid-melt and fluid-tourmaline fractionation factors indicate a slight fractionation between granitic melt and tourmaline, but the sign of  $\Delta^{11}\text{B}_{\text{melt-Tur}}$  is controversial (Fig. 2b). A  $\Delta^{11}\text{B}_{\text{melt-Tur}}$  of  $-3\text{‰}$  at 500 °C was applied by Trumbull *et al.* (2013) and Siegel *et al.* (2016), whereas Ribeiro da Costa

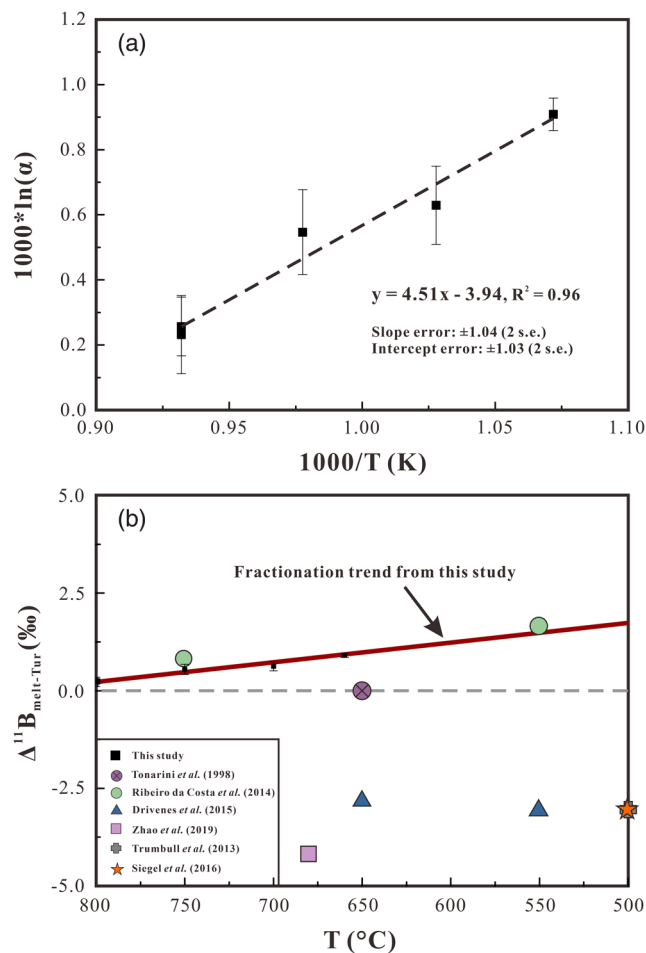


**Figure 2** (a) Boron isotopic fractionation factors between granitic melt and tourmaline versus reciprocal temperature. The dashed line represents an Ordinary Least Square regression of the five fractionation values obtained from our experiments. (b) Comparison of  $\Delta^{11}\text{B}_{\text{melt-Tur}}$  values from this study and  $\Delta^{11}\text{B}_{\text{melt-Tur}}$  applied in previous studies to interpret  $\delta^{11}\text{B}$  values analysed in tourmaline.

*et al.* (2014) used a positive factor to calculate the variation in B isotope composition of magma with tourmaline crystallisation. The inconsistency probably results from the difference in experimental and analytical methods as well as from different fluid compositions in the experimental studies on fluid-melt and fluid-tourmaline fractionation (Palmer *et al.*, 1992; Hervig *et al.*, 2002; Meyer *et al.*, 2008; Maner and London, 2018). Such problems could be overcome in this study. In addition, the composition of tourmaline formed in our experiments is similar to natural magmatic tourmaline (Figs. S-1 and S-2), which allows us to apply our results to granitic and pegmatitic systems.

## Implications for Tracing Magma Evolution with Boron Isotopes

Boron isotope fractionation is expected to occur during magmatic-hydrothermal processes due to the difference in coordination of B between melt, fluid, and B-bearing minerals. As the most common B-rich mineral in granite and pegmatite, tourmaline is widely studied to trace processes at the magmatic-hydrothermal transition by measuring its B isotope composition. The results of this study show small slightly positive temperature-dependent  $\Delta^{11}\text{B}_{\text{melt-Tur}}$  values. Thus, the B isotope composition of tourmaline crystallising from a granitic melt

could approximately reflect that of the silicate melt, especially at high temperatures (~700–800 °C). However, since the residual melt will be progressively enriched in  $^{11}\text{B}$  with ongoing crystallisation of tourmaline in a closed system, as indicated by the Rayleigh fractionation model (Fig. 3a), the  $\delta^{11}\text{B}$  of late-magmatic tourmaline should be higher than that of tourmaline crystallising at an early stage. Such an increasing trend of  $\delta^{11}\text{B}$  values from early- to late-stage tourmaline has been observed in pegmatite (Mikova *et al.*, 2010; Siegel *et al.*, 2016), based on the analysis of  $\delta^{11}\text{B}$  in core and rim of tourmalines, reflecting the evolution from early- to late-stage crystallisation. Our calculation applying a Rayleigh fractionation model and the new fractionation factors show that the consumption of ~62–78 % B in melt (as a result of tourmaline crystallisation) could explain the observed B isotopic variation of tourmaline between core and rim (Fig. 3b). Differently, some other studies reported a decrease of  $\delta^{11}\text{B}$  from early- to late-stage tourmaline in granites and pegmatites (Trumbull *et al.*, 2013; Drivenes *et al.*, 2015; Zhao *et al.*, 2019), which were ascribed to the preferential partitioning of  $^{11}\text{B}$  in tourmaline relative to the coexisting melt because negative  $\Delta^{11}\text{B}_{\text{melt-Tur}}$  values were assumed for the modelling (Fig. 3a, coloured lines). However, such an explanation is inconsistent with the positive  $\Delta^{11}\text{B}_{\text{melt-Tur}}$  value determined in this study. Alternatively, a kinetically driven B isotope fractionation during fluid exsolution is a potential interpretation for the decrease of  $\delta^{11}\text{B}$  observed in these studies (Kowalski and Wunder, 2018).

## Conclusions

We determined the temperature-dependent equilibrium B isotope fractionation between peraluminous granitic melt and tourmaline at 660 to 800 °C and 300 MPa, which can be expressed as  $\Delta^{11}\text{B}_{\text{melt-Tur}} = 4.51 \times (1000/T [\text{K}]) - 3.94$  ( $R^2 = 0.96$ ). Our experiments, for the first time, provide direct measurements of the fractionation factors that can be used for tracing B isotopes of granitic melt from the records in tourmaline.

## Acknowledgements

We thank U. Kroll, D. Qi, X. Li for their help of experiment and D. Wang for his assistance of EMPA analysis. The stay of L. Cheng at Hannover was supported by the Basic Research Fund of the Institute of Geology, China Earthquake Administration (IGCEA2018 and IGCEA1914). Laboratory costs were supported by the German Science Foundation (DFG, project HO1337/49). This paper has been greatly improved by the constructive comments from Horst R. Marschall, Vincent van Hinsberg, and an anonymous reviewer. We are also grateful to Horst R. Marschall for his editorial handling.

Editor: Horst R. Marschall

## Additional Information

Supplementary Information accompanies this letter at <https://www.geochemicalperspectivesletters.org/article2206>.



© 2022 The Authors. This work is distributed under the Creative Commons Attribution Non-Commercial No-Derivatives 4.0

License, which permits unrestricted distribution provided the original author and source are credited. The material may not be adapted (remixed, transformed or built upon) or used for commercial purposes without written permission from the

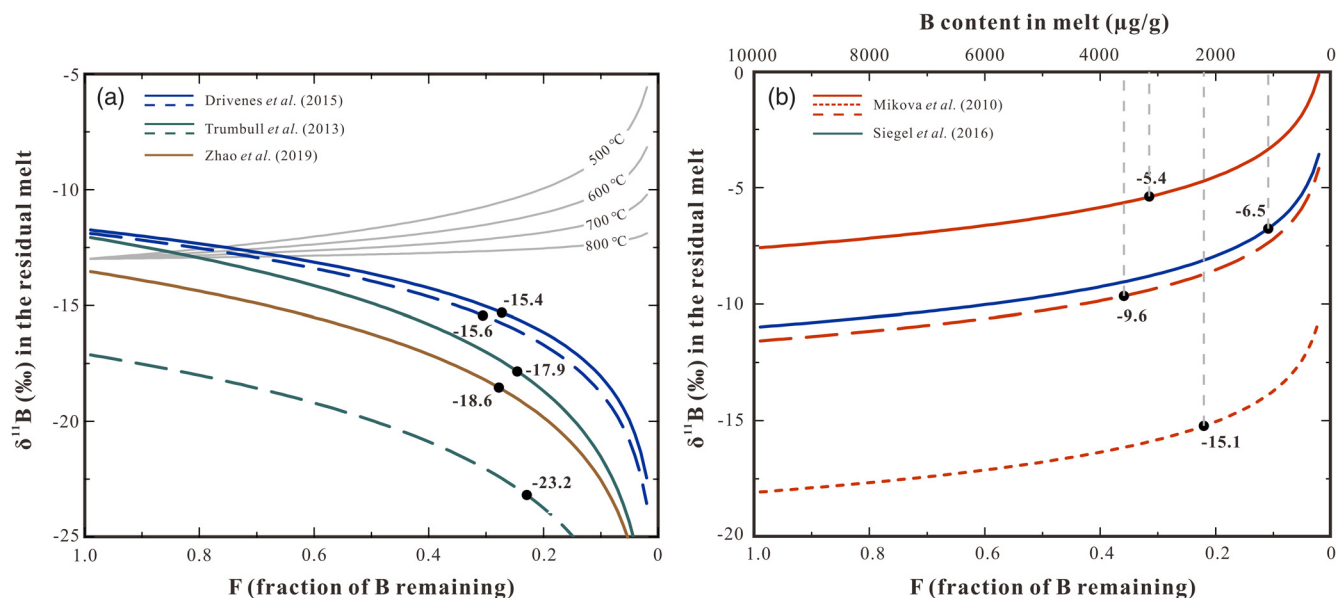


**Figure 3** (a) Modelled curves illustrating the change in  $\delta^{11}\text{B}$  values for residual melt after crystallisation of tourmaline, assuming a Rayleigh fractionation. Grey solid curves represent the evolution in  $\delta^{11}\text{B}$  assuming tourmaline crystallisation, the starting  $\delta^{11}\text{B}$  values of the melt are set as  $-13\text{‰}$  and the fractionation factors are based on the result of this study. The coloured lines are calculated  $\delta^{11}\text{B}$  variation trends of residual melts based on the  $\delta^{11}\text{B}$  analyses of zoned tourmalines and negative  $\Delta^{11}\text{B}_{\text{melt-Tur}}$  fractionation factors applied in the studies of Trumbull *et al.* (2013), Drivenes *et al.* (2015), and Zhao *et al.* (2019) (see data in Table S-8). Note the discrepancy between the grey solid lines and the coloured lines. (b) Rayleigh fractionation model illustrating the variation of  $\delta^{11}\text{B}$  of residual melt with ongoing tourmaline crystallisation using tourmaline data from Mikova *et al.* (2010) and Siegel *et al.* (2016) and the positive fractionation factors from this study. The black dots in both figures represent  $\delta^{11}\text{B}$  values of melt at the end of tourmaline crystallisation, calculated from the  $\delta^{11}\text{B}$  values determined at the rim of the tourmalines. The  $\delta^{11}\text{B}$  values at  $F = 1.0$  are calculated from  $\delta^{11}\text{B}$  values determined in the core of the tourmalines. Data used to draw the coloured lines are listed in Table S-8, and the detailed calculation process is given in SI.

author. Additional information is available at <https://www.geochemicalperspectivesletters.org/copyright-and-permissions>.

**Cite this letter as:** Cheng, L., Zhang, C., Zhou, Y., Horn, I., Weyer, S., Holtz, F. (2022) Experiments reveal enrichment of  $^{11}\text{B}$  in granitic melt resulting from tourmaline crystallisation. *Geochem. Persp. Let.* 20, 37–42. <https://doi.org/10.7185/geochemlet.2206>

## References

- DINGWELL, D.B., PICHAVANT, M., HOLTZ, F. (1996) Chapter 8. Experimental studies of boron in granitic melts. In: ANOVITZ, L.M., GREW, E.S. (Eds.) *Boron: Mineralogy, Petrology, and Geochemistry*. De Gruyter, Berlin, 331–385. <https://doi.org/10.1515/9781501509223-010>
- DRIVENES, K., LARSEN, R., MÜLLER, A., SØRENSEN, B., WIEDENBECK, M., RAANES, M. (2015) Late-magmatic immiscibility during batholith formation: assessment of B isotopes and trace elements in tourmaline from the Land's End granite, SW England. *Contributions to Mineralogy and Petrology* 169, 1–27. <https://doi.org/10.1007/s00410-015-1151-6>
- ERTL, A., HENRY, D.J., TILLMANN, E. (2018) Tetrahedral substitutions in tourmaline: a review. *European Journal of Mineralogy* 30, 465–470. <https://doi.org/10.1127/ejm/2018/0030-2732>
- HERVIG, R.L., MOORE, G.M., WILLIAMS, L.B., PEACOCK, S.M., HOLLOWAY, J.R., ROGGENSACK, K. (2002) Isotopic and elemental partitioning of boron between hydrous fluid and silicate melt. *American Mineralogist* 87, 769–774. <https://doi.org/10.2138/am-2002-5-620>
- KOWALSKI, P.M., WUNDER, B. (2018) Boron Isotope Fractionation Among Vapor–Liquids–Solids–Melts: Experiments and Atomistic Modeling. In: MARSHALL, H.R., FOSTER, G.L. (Eds.) *Boron isotopes*. Advances in Isotope Geochemistry. Springer, Cham, 33–69. [https://doi.org/10.1007/978-3-319-64666-4\\_3](https://doi.org/10.1007/978-3-319-64666-4_3)
- LI, Y.C., CHEN, W.C., WEI, H.Z., JIANG, S.Y., PALMER, M.R., VAN DE VEN, T.G.M., HOHL, S., LU, J.J., MA, J. (2020) Exploration of driving mechanisms of equilibrium boron isotope fractionation in tourmaline group minerals and fluid: A density functional theory study. *Chemical Geology* 536, 119466. <https://doi.org/10.1016/j.chemgeo.2020.119466>
- LONDON, D., MORGAN, G.B., WOLF, M.B. (1996) Chapter 7. Boron in granitic rocks and their contact aureoles. In: ANOVITZ, L.M., GREW, E.S. (Eds.) *Boron: Mineralogy, Petrology, and Geochemistry*. De Gruyter, Berlin, 299–330. <https://doi.org/10.1515/9781501509223-009>
- MANER, J.L., LONDON, D. (2018) Fractionation of the isotopes of boron between granitic melt and aqueous solution at 700 °C and 800 °C (200 MPa). *Chemical Geology* 489, 16–27. <https://doi.org/10.1016/j.chemgeo.2018.05.007>
- MARSHALL, H.R., JIANG, S.-Y. (2011) Tourmaline isotopes: no element left behind. *Elements* 7, 313–319. <https://doi.org/10.2113/gselements.7.5.313>
- MEYER, C., WUNDER, B., MEDNER, A., ROMER, R.L., HEINRICH, W. (2008) Boron-isotope fractionation between tourmaline and fluid: an experimental re-investigation. *Contributions to Mineralogy and Petrology* 156, 259–267. <https://doi.org/10.1007/s00410-008-0285-1>
- MIKOVA, J., NOVÁK, M., JANOUSEK, V. (2010) Boron isotopes in tourmalines of dravite-schorl series from granitic pegmatites of the Moldanubicum Zone, Czech Republic. *Acta Mineralogica-Petrographica Abstract Series* 6, 475.
- PALMER, M.R., LONDON, D., MORGAN, G.B., BABB, H.A. (1992) Experimental determination of fractionation of  $^{11}\text{B}/^{10}\text{B}$  between tourmaline and aqueous vapor: A temperature- and pressure-dependent isotopic system. *Chemical Geology: Isotope Geoscience section* 101, 123–129. [https://doi.org/10.1016/0009-2541\(92\)90209-N](https://doi.org/10.1016/0009-2541(92)90209-N)
- RIBEIRO DA COSTA, I., MOURÃO, C., RÉCIO, C., GUIMARÃES, F., ANTUNES, I.M., RAMOS, J.F., BARRIGA, F.J.A.S., PALMER, M.R., MILTON, J.A. (2014) Tourmaline occurrences within the Penamacor-Monsanto granitic pluton and host-rocks (Central Portugal): genetic implications of crystal-chemical and isotopic features. *Contributions to Mineralogy and Petrology* 167, 1–23. <https://doi.org/10.1007/s00410-014-0993-7>
- SIEGEL, K., WAGNER, T., TRUMBULL, R.B., JONSSON, E., MATALIN, G., WÄLLE, M., HEINRICH, C.A. (2016) Stable isotope (B, H, O) and mineral-chemistry constraints on the magmatic to hydrothermal evolution of the Varuträsk rare-element pegmatite (Northern Sweden). *Chemical Geology* 421, 1–16. <https://doi.org/10.1016/j.chemgeo.2015.11.025>
- TONARINI, S., DINI, A., PEZZOTTA, F., LEEMAN, W.P. (1998) Boron isotopic composition of zoned (schorl-elbaite) tourmalines, Mt. Capanne Li-Cs pegmatites, Elba (Italy). *European Journal of Mineralogy* 10, 941–951. <https://doi.org/10.1127/ejm/10/5/0941>
- TONARINI, S., FORTE, C., PETRINI, R., FERRARA, G. (2003) Melt/biotite  $^{11}\text{B}/^{10}\text{B}$  isotopic fractionation and the boron local environment in the structure of volcanic



- glasses. *Geochimica et Cosmochimica Acta* 67, 1863–1873. [https://doi.org/10.1016/S0016-7037\(02\)00987-0](https://doi.org/10.1016/S0016-7037(02)00987-0)
- TRUMBULL, R.B., BEURLEN, H., WIEDENBECK, M., SOARES, D.R. (2013) The diversity of B-isotope variations in tourmaline from rare-element pegmatites in the Borborema Province of Brazil. *Chemical Geology* 352, 47–62. <https://doi.org/10.1016/j.chemgeo.2013.05.021>
- WU, J., STEBBINS, J.F. (2013) Temperature and modifier cation field strength effects on aluminoborosilicate glass network structure. *Journal of Non-Crystalline Solids* 362, 73–81. <https://doi.org/10.1016/j.jnoncrysol.2012.11.005>
- ZHAO, H.D., ZHAO, K.D., PALMER, M.R., JIANG, S.Y. (2019) In-situ elemental and boron isotopic variations of tourmaline from the Sanfang granite, South China: Insights into magmatic-hydrothermal evolution. *Chemical Geology* 504, 190–204. <https://doi.org/10.1016/j.chemgeo.2018.11.013>

## Experiments reveal enrichment of $^{11}\text{B}$ in granitic melt resulting from tourmaline crystallisation

L.N. Cheng, C. Zhang, Y.S. Zhou, I. Horn, S. Weyer, F. Holtz

### Supplementary Information

The Supplementary Information includes:

- Starting Materials
- Experimental Techniques
- Analytical Methods
- Run Products and Major Element Compositions
- Rayleigh Fractionation Model
- Tables S-1 to S-8
- Figures S-1 and S-2
- Supplementary Information References

### Starting Materials

Crystallisation experiments were conducted using a B-rich peraluminous granitic glass (B10 glass). Glass synthesis and crystallisation experiments were conducted at the Leibniz University of Hannover. The nominally B-free glass (BDG-1) was produced by melting the powder of a peraluminous tourmaline-free two-mica granite from the Himalayan orogen with  $\text{Na}_2\text{O}/(\text{Na}_2\text{O} + \text{K}_2\text{O})$  of 0.45 (values in wt. %, see Table S-1). The powder was placed in a platinum crucible at 1600 °C for 2 h and then quenched. The obtained glass was then milled into fine-grained powder in an agate mortar. The melting process (same temperature) was repeated two times for achieving a homogeneous glass (BDG-1). The B-rich glass was synthesised by melting powder of BDG-1 glass with boric acid ( $\text{H}_3\text{BO}_3$ ) at 1600 °C for 2 h, and the melting process was repeated three times. The added amount of  $\text{H}_3\text{BO}_3$  was assigned to generate a target  $\text{B}_2\text{O}_3$  content of 10 wt. % in the B10 glass, but the final  $\text{B}_2\text{O}_3$  content in this glass is slightly lower (8.8 wt. %) due to loss of B during glass melting (Holtz *et al.*, 1993). However, the B content is still much higher than the  $\text{B}_2\text{O}_3$  content of peraluminous rhyolitic melts in equilibrium with tourmaline (~2 wt. % at 750 °C, 200 MPa,  $a_{\text{H}_2\text{O}} \approx 1$ ,  $f_{\text{O}_2} \approx \text{NNO}$ ) (*e.g.*, Wolf and London, 1997; London, 1999). The measured compositions of BDG-1 and B10 glasses are listed in Table S-1.

## Experimental Techniques

Fine-grained starting glass powder (<100  $\mu\text{m}$ ) was used for crystallisation experiments. The target amount of water was set as 8 wt. % for the experiments performed at 300 MPa (except for experiment DC-87, with ~10 wt. % added water). The addition of 8 wt. %  $\text{H}_2\text{O}$  is sufficient to achieve water saturation for B-free rhyolitic melt (*e.g.*, Holtz *et al.*, 2001), but the addition of  $\text{B}_2\text{O}_3$  is expected to increase the water solubility (Holtz *et al.*, 1993). Therefore, the experiments with 8 wt. %  $\text{H}_2\text{O}$  were likely slightly undersaturated in  $\text{H}_2\text{O}$ . For investigating the influence of  $a_{\text{H}_2\text{O}}$  on the B isotope fractionation, one experimental run (DC-28) with an assigned  $a_{\text{H}_2\text{O}}$  of ~0.7 was prepared by adding a fluid composed of a mixture of  $\text{H}_2\text{O}$  and  $\text{CO}_2$  (added as silver oxalate). The starting materials were loaded in gold capsules (15 mm long, 2.8 mm internal diameter, and 0.2 mm wall thickness), and subsequently sealed by arc welding. Prior to experiments, the welded capsules were kept at 110  $^\circ\text{C}$  overnight to check for leakage.

Crystallisation experiments were performed at 660 to 800  $^\circ\text{C}$  and 300 MPa in water-pressurised cold-seal pressure vessels. The run durations were 30 days at 660  $^\circ\text{C}$ , 25 days at 700  $^\circ\text{C}$ , 20 days at 750  $^\circ\text{C}$ , and 15 days at 800  $^\circ\text{C}$  (Table 1). Reverse-direction experiments were not performed here due to the negligible diffusion of tourmaline. The temperature error is expected to be less than  $\pm 10$   $^\circ\text{C}$  (Holtz *et al.*, 2004). Oxygen fugacity ( $f\text{O}_2$ ) was not controlled, but the intrinsic  $f\text{O}_2$  of the pressure vessels, made from a Ni-rich alloy, is close to the Ni-NiO buffer. Experiments were quenched isobarically with a flux of compressed air, allowing a cooling rate of ca. 300  $^\circ\text{C}$  within 1 minute (Holtz *et al.*, 2004). Quenched capsules were weighted to check for potential leakage during the experiments.

## Analytical Methods

### Electron microprobe analysis (EMPA)

Major element compositions of starting glasses and experimental products were analysed by electron microprobe analysis (EMPA) using a Cameca SX-100 microprobe at the Leibniz University of Hannover. Glasses and tourmalines were measured for Si, Ti, Al, Fe, Mn, Mg, Ca, Na, K, using 15 kV accelerating voltage, 15 nA beam current, and a spot size of 2  $\mu\text{m}$  and 10  $\mu\text{m}$  was used for tourmalines and glasses respectively. Boron and fluorine were analysed with the same accelerating voltage and spot size, but a higher beam current (100 nA) was applied. A PC3 crystal was used for detecting B. The following standards were used for calibration: jadeite (Na), MgO (Mg), orthoclase (K), wollastonite (Ca and Si),  $\text{TiO}_2$  (Ti),  $\text{Fe}_2\text{O}_3$  (Fe),  $\text{Mn}_3\text{O}_4$  (Mn), Kyanite (Al),  $\text{SrF}_2$  (F), and dravite (B). Additional details on analytical conditions with EPMA were reported in Cheng *et al.* (2019). Tourmaline structural formulas were calculated in an Excel spreadsheet on the basis of 31 anions, assuming stoichiometric amounts of  $\text{B}_2\text{O}_3$  ( $\text{B} = 3$  apfu),  $\text{H}_2\text{O}$  ( $\text{OH} + \text{F} = 4$  apfu), and  $\text{Li}_2\text{O}$  ( $\text{Li} = 15 - [\text{T} + \text{Z} + \text{Y}]$ ), and assuming that all Fe is present as  $\text{Fe}^{2+}$  (Henry and Dutrow, 1996). In order to verify the reliability of EMPA for  $\text{B}_2\text{O}_3$  content in the experimental glass, four reference glasses (B1, B4, B6, and B10 glasses with  $\text{B}_2\text{O}_3$  content of 8.54, 5.37, 3.74, and 0.94 wt. %, respectively) were analysed by both Laser ablation Inductively coupled plasma mass spectrometry (LA-ICP-MS) and EMPA, the good agreement between LA-ICPMS and



EPMA data confirms the accuracy of EPMA for B<sub>2</sub>O<sub>3</sub> contents as low as ~ 0.2 wt. % (Fig. 7a in Cheng *et al.*, 2019). In this study, the above four reference glasses were also analysed during the measurement of experimental glasses for monitoring data quality and calibrating the B<sub>2</sub>O<sub>3</sub> content data of experimental glasses. The complete datasets of experimental glasses and tourmalines are listed in Supplementary Tables S-2 and S-3, respectively.

### Laser ablation multi-collector inductively coupled plasma mass spectrometry (LA-MC-ICP-MS)

B-isotope compositions of starting glasses and experimental products were measured using a Thermo Scientific Neptune Plus which was connected to a Spectra-Physics Solstice femtosecond laser ablation system at the Leibniz University of Hannover. A detailed description of in situ B isotopic measurements is provided in Cheng *et al.* (2021). The laser was operated with a fluence of about 1 J/cm<sup>2</sup> at a repetition rate of 10 Hz with a laser spot diameter of 30 μm. The analyses on the experimental glasses were carried out in raster mode, and tourmaline measurements were performed in point or line mode (depending on the crystal size and shape). Instrumental mass bias was monitored using the standard-sample bracketing method. The tourmaline schorl (#112566, δ<sup>11</sup>B = -12.5 ± 0.05 ‰ relative to NIST SRM 951) (Dyar *et al.*, 2001) was used as bracketing standard for the B isotope analysis of both glass and tourmaline due to the similar B concentration between experimental glass (~8 wt. %) and tourmaline (~10 wt. %). B isotope composition of samples are expressed relative to NIST SRM 951 as follows:

$$\delta^{11}\text{B} = \left\{ \left[ \frac{(^{11}\text{B}/^{10}\text{B})_{\text{sample}}}{(^{11}\text{B}/^{10}\text{B})_{\text{NIST SRM 951}}} \right] - 1 \right\} \times 1000 \quad \text{Eq. S-1}$$

B isotope ratios of all samples were determined as δ<sup>11</sup>B values relative to tourmaline schorl and recalculated relative to NIST SRM 951 using the following equation:

$$\delta^{11}\text{B} = \delta^{11}\text{B}_{\text{sample/schorl}} + \delta^{11}\text{B}_{\text{schorl/NIST SRM 951}} + (\delta^{11}\text{B}_{\text{sample/schorl}} \times \delta^{11}\text{B}_{\text{schorl/NIST SRM 951}})/1000 \quad \text{Eq. S-2}$$

where δ<sup>11</sup>B<sub>sample/schorl</sub> is the measured δ<sup>11</sup>B value of the sample relative to schorl (#112566), and δ<sup>11</sup>B<sub>schorl/NIST SRM 951</sub> is the δ<sup>11</sup>B value of the schorl (#112566) relative to NIST SRM 951. The repeatability of the data was monitored using tourmaline dravite (#108796, δ<sup>11</sup>B = -6.6 ± 0.1 ‰) and elbaite (#98144, δ<sup>11</sup>B = -10.4 ± 0.2 ‰) (Dyar *et al.*, 2001). The dravite and elbaite yields an average δ<sup>11</sup>B value of -5.3 ± 0.1 ‰ (2 s.d., n = 6) and -11.0 ± 0.2 ‰ (2 s.d., n = 13), respectively, in this study (Table S-4). The analytical precision is estimated to be better than 0.2 ‰ based on replicate analyses of monitored tourmalines. The B-isotope compositions of starting glasses and experimental products are listed in Supplementary Tables S-5–S-7.

B isotopic fractionation factors between granitic melt and tourmaline can be expressed with α and Δ notation as:

$$\alpha = \frac{(^{11}\text{B}/^{10}\text{B})_{\text{melt}}}{(^{11}\text{B}/^{10}\text{B})_{\text{Tur}}} \quad \text{Eq. S-3}$$

$$\Delta^{11}\text{B}_{\text{melt-Tur}} = \delta^{11}\text{B}_{\text{melt}} - \delta^{11}\text{B}_{\text{Tur}}. \quad \text{Eq. S-4}$$



The above two terms can be related using the following expression:

$$1000\ln(\alpha) \approx \Delta^{11}\text{B}. \quad \text{Eq. S-5}$$

## Run Products and Major Element Compositions

Microscopic observation and mass-balance calculation show that the amount of tourmaline in experiments increases with decreasing experimental temperature. Biotite was not observed in the experimental products, indicating that tourmaline is the main ferromagnesian mineral. Bubbles were found in runs DC-28 and DC-87, and we propose that the occurrence of bubbles in the former run resulted from the addition of CO<sub>2</sub> in the form of silver oxalate, whereas the bubbles of the latter run were mainly composed of water because this run was saturated in water.

There is no large variation in composition of glasses because tourmaline is the main mineral phase in all experimental runs. The Al<sub>2</sub>O<sub>3</sub>, FeO, and MgO contents of glasses decrease with decreasing temperature, which is due to a higher proportion of tourmaline with decreasing temperature. It can be noted that B<sub>2</sub>O<sub>3</sub> contents are much higher than those determined by Wolf and London (1997) from experiments in which tourmaline was coexisting with melt and other residual minerals (partial melting experiments), including especially biotite and/or cordierite. In this study, nearly all the Fe and Mg present in the peraluminous system is incorporated in the tourmaline phase. The high B<sub>2</sub>O<sub>3</sub> contents in the melts can be explained by the absence of other ferromagnesian phases in our experiments, which is in agreement with observations of London (1999) who concluded that peraluminous granitic systems that only contain tourmaline as ferromagnesian phases (*e.g.*, Fe/Mg ratios not buffered by biotite) can contain extremely high B<sub>2</sub>O<sub>3</sub> contents.

As revealed by EPMA data (Table S-3), tourmalines from all experiments are rich in Fe relative to Mg, with molar Mg/(Mg + Fe) within 0.35–0.55, which is consistent with that of natural magmatic tourmalines (Figs. S-1 and S-2). For the high-temperature experiments (800 °C), all analytical data of tourmaline plot in the area of schorl, but the composition varies towards the dravite end member with decreasing temperature (Fig. S-2a). The other element concentrations (such as Al, Ti, Na, and Ca) of tourmaline do not show any correlation with temperature (Figs. S-1 and S-2).

Some tourmaline grains display well-developed hourglass sector zoning patterns (Fig. 1e, f). Hourglass sector zoning has been identified in natural (*e.g.*, van Hinsberg *et al.*, 2006) and experimental tourmalines (Maner *et al.*, 2019), which was considered as a result of mineral's asymmetric polar properties and could result in a compositional variation in different sectors (van Hinsberg *et al.*, 2006). In the cross-section parallel to the *c* axis, three zones can be recognised in BSE images: *c*+, *c*−, and *a* sectors (Fig. 1e). And in the cross-section perpendicular to the *c* axis, the tourmaline is divided into two compositional sectors (Fig. 1f), which is likely related to the growth on the *m* and *a* faces. The *c*+ sector is Ca- and Ti-poor and Mg-rich relative to the *c*− sector, and the light sector in the cross-section perpendicular to the *c*-axis contains higher Ti and Fe but lower Al compared with the dark sector (Fig. S-2). Van Hinsberg and Marschall (2007) first observed a small fractionation of B isotope between different sectors ( $\Delta^{11}\text{B}_{c-/c+} < 1.8 \pm 0.6 \text{ ‰}$ ) in natural



metamorphic sector-zoned tourmaline, they attributed this fractionation to the local variations in host medium along the growth surface resulting from preferred uptake of elements, and they suggested that the composition of *a* sector could represent the composition of environment where tourmaline formed. Similar fractionation ( $\Delta^{11}\text{B}_{c-/c+} \approx 1.5 \text{ ‰}$ ) was also found in metasomatic tourmaline by Trumbull *et al.* (2009). In this study, Due to the small size of the synthesised tourmaline (<100  $\mu\text{m}$  long and <50  $\mu\text{m}$  wide) and the large beam size of the laser ( $\sim 30 \mu\text{m}$ , but most analyses on the experimental tourmaline were carried out in line mode), the analyses cannot only focus on the *a* sector. However, there are good reasons to believe that the sector zoning effect on the B isotope data of tourmaline in this study could be neglected. First, van Hinsberg and Marschall (2007) observed that the  $\Delta^{11}\text{B}_{c-/c+}$  value decreases from the core to the rim of the tourmaline grain, since the tourmaline grain shows prograde growth, they concluded that the sector zoning effect on  $\delta^{11}\text{B}$  decreases with increasing temperature. The  $\Delta^{11}\text{B}_{c-/c+}$  value at the rim lower than 0.5 ‰ (close to the measurement error of the SIMS), combining a formation temperature of about 600 °C for the rim (calculated by the single crystal thermometer from van Hinsberg and Schumacher (2007), the sector zoning effect on  $\delta^{11}\text{B}$  probably very small when the formation temperature of tourmaline exceeds 600 °C. Second, the analytical points are randomly distributed in the tourmaline grains, but the  $\delta^{11}\text{B}$  value of B isotope composition of tourmalines formed in given temperature experiment is identical, with a standard deviation lower than 0.1 ‰ (Table S-7), suggesting that the measurement location did not impact the B isotope composition results of tourmaline, even though it shows obvious sector zoning.

## Rayleigh Fractionation Model

The B isotope fractionation of the residual melt with tourmaline crystallisation or fluid exsolution in a closed system can be modelled using a Rayleigh fractionation law:

$$\delta^{11}\text{B}_f = (\delta^{11}\text{B}_i + 1000) \times F^{\alpha-1} - 1000 \quad \text{Eq. S-6}$$

where  $F$  is the fraction of B remaining in the melt,  $\alpha$  is the temperature-dependent B isotope fractionation factor, which can be calculated using Equation S-5.  $\delta^{11}\text{B}_f$  and  $\delta^{11}\text{B}_i$  are the final and initial B isotope compositions of the melt, respectively. The  $\delta^{11}\text{B}$  values of melt can be calculated by:

$$\delta^{11}\text{B}_m = \delta^{11}\text{B}_{\text{tur}} + \Delta^{11}\text{B}_{\text{melt-Tur}} \quad \text{Eq. S-7}$$

where  $\delta^{11}\text{B}_{\text{Tur}}$  is the B isotope compositions of the tourmaline coexisting with melt,  $\Delta^{11}\text{B}_{\text{melt-Tur}}$  is the B isotope fractionation between melt and tourmaline.



## Supplementary Tables

**Table S-1** Average major element compositions (wt. %) of synthesised glasses recalculated on an anhydrous basis (from Cheng *et al.*, 2019). Total iron content is expressed as Fe<sup>2+</sup>.

Element	BFG-1	B10
SiO <sub>2</sub>	74.09	68.18
TiO <sub>2</sub>	0.14	0.13
Al <sub>2</sub> O <sub>3</sub>	15.17	13.58
FeO	1.19	1.15
MnO	0.03	0.03
MgO	0.27	0.19
CaO	0.88	0.82
Na <sub>2</sub> O	3.69	3.44
K <sub>2</sub> O	4.53	3.72
B <sub>2</sub> O <sub>3</sub>	0.00	8.76
F	n.d.	n.d.
Total	99.06	97.54

**Table S-2** Average major element compositions (wt. %), modal compositional end members, and ASI of experimental glasses. Total iron content is expressed as Fe<sup>2+</sup>. H<sub>2</sub>O content is calculated as 100 – total. Numbers in parentheses are standard deviations.

Element	DC-27 glass (n = 8)	DC-28 glass (n = 7)	DC-10 glass (n = 10)	DC-11 glass (n = 10)	DC-87 glass (n = 10)
SiO <sub>2</sub>	62.76 (0.45)	64.97 (0.39)	64.95 (0.36)	62.69 (0.14)	64.37 (0.29)
TiO <sub>2</sub>	0.11 (0.02)	0.12 (0.02)	0.08 (0.01)	0.09 (0.01)	0.08 (0.02)
Al <sub>2</sub> O <sub>3</sub>	12.19 (0.08)	12.03 (0.17)	11.60 (0.14)	11.47 (0.11)	11.27 (0.11)
FeO	0.79 (0.05)	0.74 (0.04)	0.53 (0.04)	0.78 (0.04)	0.32 (0.03)
MnO	0.03 (0.01)	0.03 (0.02)	0.03 (0.03)	0.02 (0.02)	0.04 (0.03)
MgO	0.18 (0.03)	0.12 (0.03)	0.08 (0.04)	0.11 (0.05)	0.07 (0.02)
CaO	0.72 (0.03)	0.74 (0.05)	0.76 (0.04)	0.73 (0.03)	0.71 (0.02)
Na <sub>2</sub> O	2.47 (0.11)	2.85 (0.10)	3.16 (0.06)	2.77 (0.15)	2.52 (0.11)
K <sub>2</sub> O	3.26 (0.05)	3.46 (0.07)	3.64 (0.06)	3.39 (0.04)	3.40 (0.04)
B <sub>2</sub> O <sub>3</sub>	7.8 (0.2)	8.0 (0.2)	8.0 (0.1)	7.8 (0.1)	7.7 (0.2)
F	0.03 (0.02)	0.04 (0.02)	0.03 (0.02)	0.03 (0.02)	0.02 (0.02)
Total	90.35	93.11	92.87	89.89	90.50
H <sub>2</sub> O	9.69	6.88	7.17	10.15	9.47
Qtz	40.63	38.58	35.92	38.07	42.15
An	4.32	4.32	4.42	4.42	4.00
Ab	25.30	28.35	31.56	28.60	25.81
Or	23.34	24.05	25.35	24.41	24.29
ASI	1.37	1.23	1.10	1.20	1.24

**Table S-3** Major element compositions of experimental tourmalines.

Element	DC-27	DC-28	DC-10			DC-11			DC-87		
	(n = 8)	(n = 8)	Core (n = 5)	Dark (n = 4)	Light (n = 5)	Core (n = 4)	Dark (n = 2)	Light (n = 7)	a (n = 2)	c+ (n = 7)	c- (n = 2)
SiO <sub>2</sub>	33.84	32.74	34.55	31.95	32.53	35.16	33.46	33.23	35.22	33.65	32.99
TiO <sub>2</sub>	0.55	0.83	0.74	0.74	1.04	0.77	0.88	1.44	0.45	0.38	0.66
Al <sub>2</sub> O <sub>3</sub>	33.11	33.86	32.63	36.06	33.53	34.46	37.85	35.45	29.87	34.74	32.72
FeO	11.05	10.05	9.84	9.16	10.66	7.92	6.71	8.16	9.99	8.35	10.19
MnO	0.02	0.01	0.03	0.00	0.03	0.02	0.04	0.01	0.03	0.04	0.02
MgO	4.07	4.27	4.45	3.60	3.78	4.60	3.88	3.76	6.36	4.90	4.84
CaO	1.10	1.64	1.10	1.87	1.78	0.89	1.45	1.51	0.80	1.34	1.57
Na <sub>2</sub> O	1.36	1.35	1.38	1.24	1.28	1.39	1.01	1.14	1.93	1.51	1.48
K <sub>2</sub> O	0.06	0.06	0.06	0.05	0.06	0.04	0.04	0.04	0.08	0.07	0.05
B <sub>2</sub> O <sub>3</sub> <sup>#</sup>	10.48	10.71	10.11	10.72	10.23	9.90	10.41	10.01	10.02	10.08	10.07
F	0.02	0.01	0.10	0.04	0.15	0.00	0.08	0.12	0.02	0.09	0.12
Total	95.66	95.55	94.98	95.45	95.08	95.15	95.81	94.87	94.76	95.15	94.72
H <sub>2</sub> O <sup>*</sup>	3.54	3.54	3.52	3.54	3.45	3.64	3.63	3.55	3.53	3.55	3.47
B <sub>2</sub> O <sub>3</sub> <sup>*</sup>	10.29	10.27	10.34	10.33	10.22	10.56	10.64	10.45	10.25	10.42	10.21
Li <sub>2</sub> O <sup>*</sup>	0.05	0.15	0.19	0.27	0.20	0.32	0.41	0.41	0.00	0.19	0.07
Total	99.05	98.80	98.92	98.87	98.72	99.77	100.09	99.27	98.53	99.24	98.39
O=F	0.01	0.01	0.04	0.02	0.06	0.00	0.04	0.05	0.01	0.04	0.05
Total <sup>*</sup>	99.04	98.79	98.88	98.85	98.65	99.77	100.05	99.22	98.52	99.20	98.34
<i>T site</i>											
Si	5.72	5.54	5.81	5.38	5.53	5.79	5.47	5.53	5.97	5.61	5.62
Al	0.28	0.46	0.19	0.62	0.47	0.21	0.53	0.47	0.03	0.39	0.38
<i>Z site</i>											
Al	6.00	6.00	6.00	6.00	6.00	6.00	6.00	6.00	5.94	6.00	6.00
Mg	0.00	0.00	0.00	0.00	0.00	0.00	0.00	0.00	0.06	0.00	0.00

Table S-3 continued

Element	DC-27	DC-28	DC-10			DC-11			DC-87		
	(n = 8)	(n = 8)	Core (n = 5)	Dark (n = 4)	Light (n = 5)	Core (n = 4)	Dark (n = 2)	Light (n = 7)	a (n = 2)	c+ (n = 7)	c- (n = 2)
<i>Y site</i>											
Al	0.31	0.29	0.28	0.53	0.25	0.47	0.75	0.48	0.00	0.44	0.19
Ti	0.07	0.11	0.09	0.09	0.13	0.10	0.11	0.18	0.06	0.05	0.08
Mg	1.02	1.08	1.11	0.90	0.96	1.13	0.94	0.93	1.54	1.22	1.23
Mn	0.00	0.00	0.00	0.00	0.00	0.00	0.01	0.00	0.00	0.01	0.00
Fe <sup>2+</sup>	1.56	1.42	1.38	1.29	1.52	1.09	0.92	1.13	1.42	1.16	1.45
Li*	0.03	0.10	0.13	0.19	0.14	0.21	0.27	0.28	0.00	0.13	0.05
B*	3.00	3.00	3.00	3.00	3.00	3.00	3.00	3.00	3.02	3.00	3.00
<i>X site</i>											
Ca	0.20	0.30	0.20	0.34	0.32	0.16	0.25	0.27	0.15	0.24	0.29
Na	0.45	0.44	0.45	0.40	0.42	0.44	0.32	0.37	0.63	0.49	0.49
K	0.01	0.01	0.01	0.01	0.01	0.01	0.01	0.01	0.02	0.02	0.01
Xv	0.34	0.25	0.34	0.25	0.24	0.39	0.42	0.35	0.20	0.26	0.21
<i>W site</i>											
OH*	3.99	3.99	3.95	3.98	3.92	4.00	3.96	3.94	3.99	3.95	3.94
F	0.01	0.01	0.05	0.02	0.08	0.00	0.04	0.06	0.01	0.05	0.06
Total Al	6.59	6.75	6.47	7.15	6.72	6.68	7.29	6.95	5.97	6.83	6.57
$\frac{\text{Mg}}{(\text{Mg} + \text{Fe})}$	0.40	0.43	0.45	0.41	0.39	0.51	0.51	0.45	0.52	0.51	0.46
$\frac{\text{Na}}{(\text{Na} + \text{Ca})}$	0.69	0.60	0.69	0.54	0.56	0.74	0.56	0.58	0.81	0.67	0.63
$\frac{\text{Xv}}{(\text{Na} + \text{Xv})}$	0.43	0.36	0.43	0.38	0.36	0.47	0.57	0.49	0.24	0.34	0.30
Na + K	0.46	0.46	0.46	0.42	0.44	0.45	0.33	0.38	0.65	0.50	0.50

#Measured B<sub>2</sub>O<sub>3</sub> content in experimental tourmalines.

\*H<sub>2</sub>O, B<sub>2</sub>O<sub>3</sub>, and Li<sub>2</sub>O contents calculated for experimental tourmalines based on crystal chemistry.



**Table S-4** Summary of boron isotopic analyses of reference tourmalines. IMF, instrumental mass fractionation.

Standard	$^{11}\text{B}/^{10}\text{B}$	IMF	$\delta^{11}\text{B}$ vs. 951 (‰)	s.e. (2 $\sigma$ ) (‰)
<i>Elbaite 98144 (<math>^{11}\text{B}/^{10}\text{B} = 4.001</math> and <math>\delta^{11}\text{B} = -10.5</math>)</i>				
031218_Elbaite_003	4.4694	1.1171	-11.18	0.05
031218_Elbaite_005	4.4629	1.1154	-11.17	0.08
031218_Elbaite_007	4.4742	1.1183	-11.22	0.08
031218_Elbaite_083	4.4530	1.1130	-11.07	0.04
031218_Elbaite_086	4.4530	1.1130	-11.05	0.04
041218_Elbaite_002	4.4684	1.1168	-10.98	0.03
041218_Elbaite_004	4.4640	1.1157	-11.10	0.03
041218_Elbaite_006	4.4607	1.1149	-11.06	0.03
041218_Elbaite_056	4.4717	1.1176	-11.01	0.03
041218_Elbaite_115	4.4577	1.1142	-10.95	0.03
041218_Elbaite_118	4.4664	1.1163	-11.09	0.03
041218_Elbaite_141	4.4730	1.1180	-10.88	0.03
041218_Elbaite_156	4.4592	1.1145	-10.88	0.03
<i>Dravite 108796 (<math>^{11}\text{B}/^{10}\text{B} = 4.017</math> and <math>\delta^{11}\text{B} = -6.6</math>)</i>				
031218_Dravite_009	4.4952	1.1190	-5.27	0.05
031218_Dravite_011	4.4962	1.1193	-5.39	0.04
031218_Dravite_013	4.4970	1.1195	-5.33	0.04
041218_Dravite_008	4.4929	1.1185	-5.35	0.03
041218_Dravite_010	4.5093	1.1226	-5.39	0.03
041218_Dravite_012	4.5091	1.1225	-5.35	0.03

**Table S-5** Summary of LA-MC-ICP-MS boron isotope data of synthesised glasses.

Analysis no.	$^{11}\text{B}/^{10}\text{B}$	$\delta^{11}\text{B}$	s.e. (2 $\sigma$ )	$\delta^{11}\text{B}$ vs. 951 (‰)	s.d. (‰)
B10 glass-1	4.5224	13.54	0.03	0.87	
B10 glass-2	4.5209	13.61	0.03	0.94	
B10 glass-3	4.5147	13.58	0.03	0.91	
B10 glass-4	4.5189	13.59	0.03	0.92	
B10 glass-5	4.4969	13.63	0.03	0.96	
Average				0.92	0.03



**Table S-6** Summary of LA-MC-ICP-MS boron isotope data of experimental glasses.

Analysis no.	$^{11}\text{B}/^{10}\text{B}$	$\delta^{11}\text{B}$ (‰)	s.e. ( $2\sigma$ ) (‰)	$\delta^{11}\text{B}$ vs. 951 (‰)
<i>DC-27</i>				
DC-27 glass-1	4.5305	13.70	0.04	1.03
DC-27 glass-2	4.5259	13.79	0.04	1.12
DC-27 glass-3	4.5332	13.83	0.03	1.16
DC-27 glass-4	4.5287	13.67	0.03	1.00
DC-27 glass-5	4.5283	13.85	0.03	1.18
<i>DC-28</i>				
DC-28 glass-1	4.5050	13.76	0.05	1.09
DC-28 glass-2	4.5137	13.81	0.05	1.14
DC-28 glass-3	4.5097	13.77	0.05	1.10
DC-28 glass-4	4.5089	13.78	0.05	1.11
DC-28 glass-5	4.5043	13.75	0.04	1.08
<i>DC-10</i>				
DC-10 glass-1	4.5150	13.69	0.04	1.02
DC-10 glass-2	4.5128	13.61	0.04	0.94
DC-10 glass-3	4.5102	13.54	0.05	0.87
DC-10 glass-4	4.5154	13.74	0.04	1.07
DC-10 glass-5	4.5138	13.54	0.04	0.87
DC-10 glass-6	4.5130	13.68	0.04	1.01
<i>DC-11</i>				
DC-11 glass-1	4.5203	13.58	0.05	0.91
DC-11 glass-2	4.5235	13.60	0.05	0.93
DC-11 glass-3	4.5256	13.65	0.05	0.98
DC-11 glass-4	4.5180	13.57	0.05	0.90
DC-11 glass-5	4.5194	13.60	0.05	0.93
<i>DC-87</i>				
DC-87 glass-1	4.5203	13.38	0.03	0.71
DC-87 glass-2	4.5132	13.48	0.03	0.81
DC-87 glass-3	4.5114	13.50	0.03	0.83
DC-87 glass-4	4.5096	13.45	0.03	0.78
DC-87 glass-5	4.5129	13.47	0.03	0.80
DC-87 glass-6	4.5242	13.45	0.03	0.78
DC-87 glass-7	4.5205	13.43	0.03	0.76



**Table S-7** Summary of LA-MC-ICP-MS boron isotope data of experimental tourmalines.

Analysis no.	$^{11}\text{B}/^{10}\text{B}$	$\delta^{11}\text{B}$ (‰)	s.e. (2 $\sigma$ ) (‰)	$\delta^{11}\text{B}$ vs. 951(‰)
<i>DC-27</i>				
DC-27 Tur1	4.5939	13.65	0.05	0.98
DC-27 Tur2	4.5911	13.46	0.07	0.79
DC-27 Tur3	4.6237	13.61	0.10	0.94
DC-27 Tur4	4.4998	13.41	0.06	0.74
<i>DC-28</i>				
DC-28 Tur1	4.5638	13.53	0.04	0.86
DC-28 Tur2	4.6346	13.54	0.07	0.87
DC-28 Tur3	4.5985	13.65	0.08	0.98
DC-28 Tur4	4.4655	13.46	0.05	0.79
DC-28 Tur5	4.5603	13.40	0.04	0.73
<i>DC-10</i>				
DC-10 Tur1	4.5294	13.23	0.06	0.56
DC-10 Tur2	4.5156	13.16	0.04	0.50
DC-10 Tur3	4.5238	12.98	0.05	0.32
DC-10 Tur4	4.4803	12.98	0.05	0.32
<i>DC-11</i>				
DC-11 Tur1	4.5227	13.04	0.05	0.38
DC-11 Tur2	4.5169	13.12	0.04	0.46
DC-11 Tur3	4.5135	12.88	0.04	0.22
DC-11 Tur4	4.5162	12.84	0.05	0.18
<i>DC-87</i>				
DC-87 Tur1	4.5174	12.59	0.08	-0.07
DC-87 Tur2	4.5157	12.55	0.03	-0.11
DC-87 Tur3	4.5127	12.49	0.06	-0.17
DC-87 Tur4	4.5347	12.55	0.04	-0.11



**Table S-8** Boron isotopic compositions of different stage tourmalines assuming boron isotopic fractionation factors from the literature. The tourmaline data and the fractionation factors in this table are used to draw the evolution of  $\delta^{11}\text{B}$  in the melt with ongoing crystallisation of tourmaline in Figure 3.

$\delta^{11}\text{B}$ Tur core (early stage) (‰)	$\delta^{11}\text{B}$ Tur rim (late stage) (‰)	$\Delta^{11}\text{B}_{\text{melt-Tur}}$ (‰)	$T$ (°C)	Reference
-8.9	-12.6	-2.8	650	Drivenes <i>et al.</i> (2015)
-8.9	-12.6	-3.0	550	
-9.1	-14.9	-3	500	Trumbull <i>et al.</i> (2013)
-13.9	-20.2			
-9.3	-14.4	-4.2	680	Zhao <i>et al.</i> (2019)
-20	-17			
-9.5	-7.3	1.9*	500	Mikova <i>et al.</i> (2010)
-13.5	-11.5			
-12.9	-8.4	1.9*	500	Siegel <i>et al.</i> (2016)

\*Fractionation factor from this experimental study.



Supplementary Figures

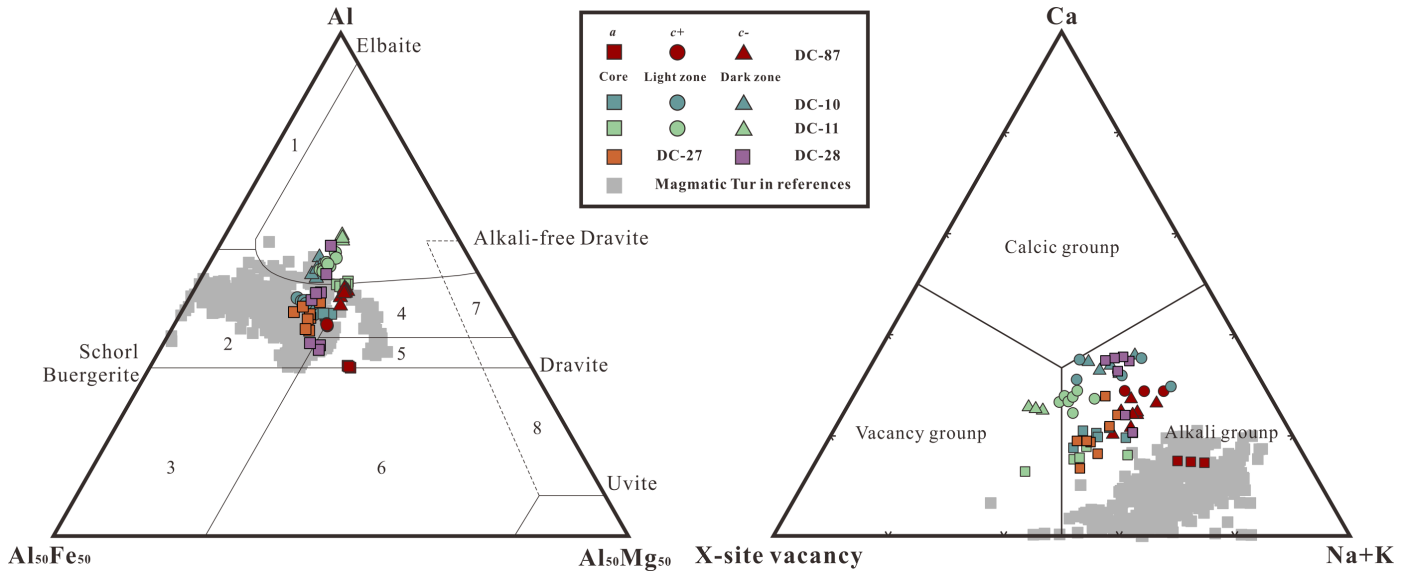


**Figure S-1** (a) Al-Fe-Mg ternary classification diagrams of tourmalines after Henry and Guidotti (1985). Labelled fields are: (1) Li-rich granitoids, pegmatites, and aplites; (2) Li-poor granitoids, pegmatites, and aplites; (3) Fe<sup>3+</sup>-rich quartz-tourmaline rocks (altered granitoids); (4) metapelites and metapsammites with Al-saturating phase; (5) metapelites and metapsammites lacking Al-saturating phase; (6) Fe<sup>3+</sup>-rich quartz-tourmaline rocks, calcisilicate rocks, and metapelites; (7) low-Ca metaultramafic rocks and Cr-V-rich metasediments; and (8) metacarbonates and metapyroxenites. (b) Ternary diagram of tourmaline groups based on X site occupancy (Hawthorne and Henry, 1999). Data sources for natural magmatic tourmalines: Ribeiro da Costa *et al.* (2014), Huang *et al.* (2016), Albert *et al.* (2018), Harlaux *et al.* (2020), Li *et al.* (2020), Cheng *et al.* (2021), Zhao *et al.* (2021).

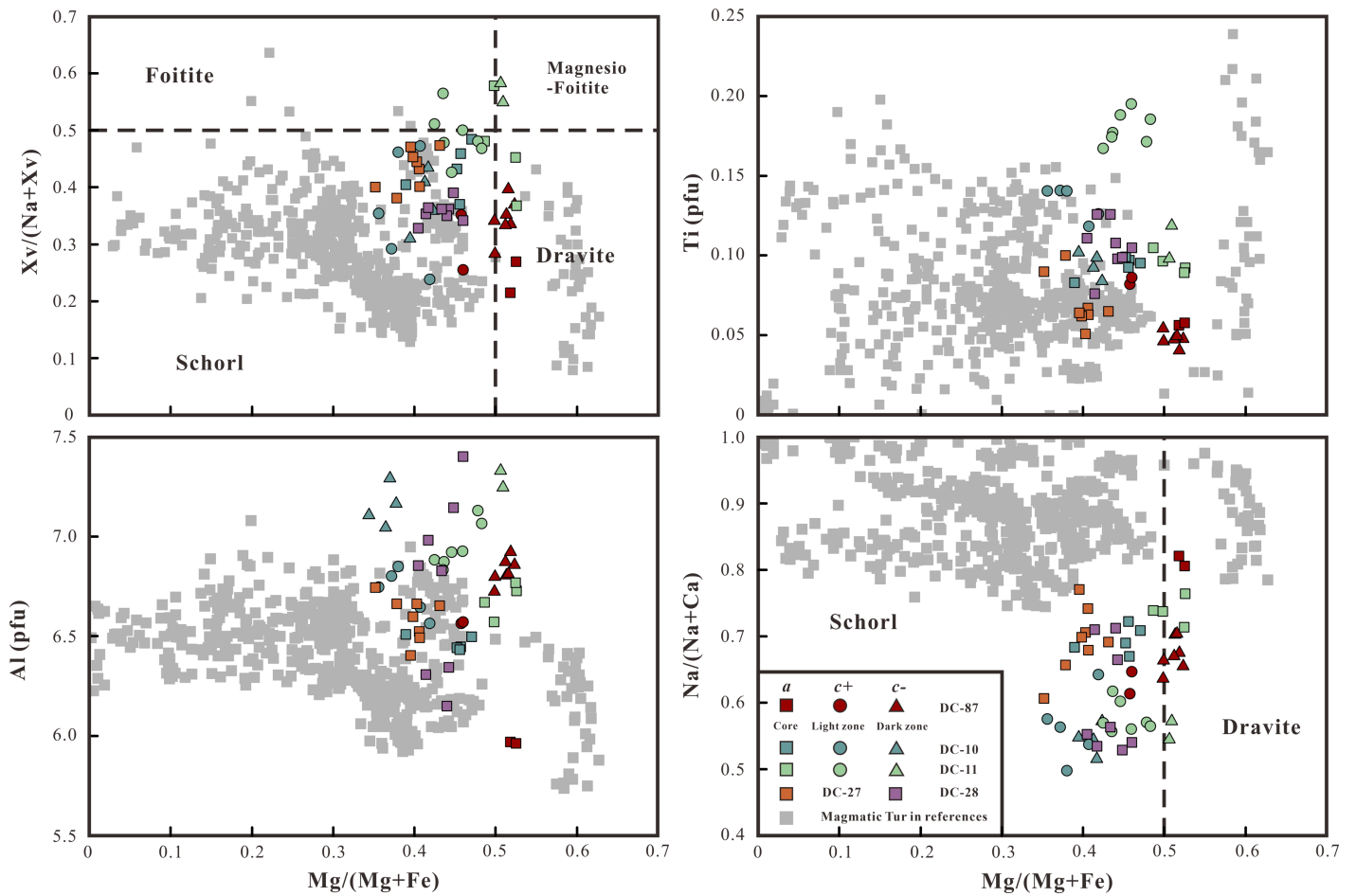


**Figure S-2** Chemical compositions of experimental tourmalines in this study and natural magmatic tourmalines expressed in terms of (a) Mg/(Mg + Fe) vs. Xv/(Na + Xv), (b) Mg/(Mg + Fe) vs. Ti (apfu), (c) Mg/(Mg + Fe) vs. Al (apfu), and (d) Mg/(Mg + Fe) vs. Na/(Na + Ca). Xv, X site vacancy. Data sources for natural magmatic tourmalines: Ribeiro da Costa *et al.* (2014), Huang *et al.* (2016), Albert *et al.* (2018), Harlaux *et al.* (2020), Li *et al.* (2020), Cheng *et al.* (2021), Zhao *et al.* (2021).

## Supplementary Information References

- Albert, C., Lana, C., Gerdes, A., Schannor, M., Narduzzi, F., Queiroga, G. (2018) Archean magmatic-hydrothermal fluid evolution in the Quadrilátero Ferrífero (SE Brazil) documented by B isotopes (LA MC-ICPMS) in tourmaline. *Chemical Geology* 481, 95–109. <https://doi.org/10.1016/j.chemgeo.2018.02.002>
- Cheng, L., Zhang, C., Li, X., Almeev, R.R., Yang, X., Holtz, F. (2019) Improvement of Electron Probe Microanalysis of Boron Concentration in Silicate Glasses. *Microscopy and Microanalysis* 25, 874–882. <https://doi.org/10.1017/S1431927619014612>
- Cheng, L., Zhang, C., Liu, X., Yang, X., Zhou, Y., Horn, I., Weyer, S., Holtz, F. (2021) Significant boron isotopic fractionation in the magmatic evolution of Himalayan leucogranite recorded in multiple generations of tourmaline. *Chemical Geology* 571, 120194. <https://doi.org/10.1016/j.chemgeo.2021.120194>
- Drivenes, K., Larsen, R., Müller, A., Sørensen, B., Wiedenbeck, M., Raanes, M. (2015) Late-magmatic immiscibility during batholith formation: assessment of B isotopes and trace elements in tourmaline from the Land's End granite, SW England. *Contributions to Mineralogy and Petrology* 169, 1–27. <https://doi.org/10.1007/s00410-015-1151-6>
- Dyar, M.D., Wiedenbeck, M., Robertson, D., Cross, L.R., Delaney, J.S., Ferguson, K., Francis, C.A., Grew, E.S., Guidotti, C.V., Hervig, R.L. (2001) Reference minerals for the microanalysis of light elements. *Geostandards and Geoanalytical Research* 25, 441–463. <https://doi.org/10.1111/j.1751-908X.2001.tb00616.x>
- Harlaux, M., Kouzmanov, K., Gialli, S., Laurent, O., Rielli, A., Dini, A., Chauvet, A., Menzies, A., Kalinaj, M., Fontboté, L. (2020) Tourmaline as a Tracer of Late-Magmatic to Hydrothermal Fluid Evolution: The World-Class San Rafael Tin (-Copper) Deposit, Peru. *Economic Geology* 115, 1665–1697. <https://doi.org/10.5382/econgeo.4762>
- Hawthorne, F.C., Henry, D.J. (1999) Classification of the minerals of the tourmaline group. *European Journal of Mineralogy* 11, 201–215. <https://doi.org/10.1127/ejm/11/2/0201>
- Henry, D.J., Dutrow, B.L. (1996) Chapter 10. Metamorphic tourmaline and its petrologic applications. In: Anovitz, L.M., Grew, E.S. (Eds.) *Boron: Mineralogy, Petrology, and Geochemistry*. De Gruyter, Berlin, 503–557. <https://doi.org/10.1515/9781501509223-012>
- Henry, D.J., Guidotti, C.V. (1985) Tourmaline as a petrogenetic indicator mineral: an example from the staurolite-grade metapelites of NW Maine. *American Mineralogist* 70, 1–15.
- Holtz, F., Dingwell, D.B., Behrens, H. (1993) Effects of F, B<sub>2</sub>O<sub>3</sub> and P<sub>2</sub>O<sub>5</sub> on the solubility of water in haplogranite melts compared to natural silicate melts. *Contribution to Mineralogy and Petrology* 113, 492–501. <https://doi.org/10.1007/BF00698318>
- Holtz, F., Johannes, W., Tamic, N., Behrens, H. (2001) Maximum and minimum water contents of granitic melts generated in the crust: a reevaluation and implications. *Lithos* 56, 1–14. [https://doi.org/10.1016/S0024-4937\(00\)00056-6](https://doi.org/10.1016/S0024-4937(00)00056-6)
- Holtz, F., Sato, H., Lewis, J., Behrens, H., Nakada, S. (2004) Experimental Petrology of the 1991–1995 Unzen Dacite, Japan. Part I: Phase Relations, Phase Composition and Pre-eruptive Conditions. *Journal of Petrology* 46, 319–337. <https://doi.org/10.1093/petrology/egh077>
- Huang, S., Song, Y., Hou, Z., Xue, C. (2016) Chemical and stable isotopic (B, H, and O) compositions of tourmaline in the Maocaooping vein-type Cu deposit, western Yunnan, China: Constraints on fluid source and evolution. *Chemical Geology* 439, 173–188. <https://doi.org/10.1016/j.chemgeo.2016.06.031>
- Li, J., Fan, W., Zhang, L., Ding, L., Yue, Y., Xie, J., Cai, F., Sein, K. (2020) B-rich melt immiscibility in Late Cretaceous Nattaung granite, Myanmar: Implication by composition and B isotope in tourmaline. *Lithos* 356–357, 105380. <https://doi.org/10.1016/j.lithos.2020.105380>
- London, D. (1999) Stability of tourmaline in peraluminous granite systems: the boron cycle from anatexis to hydrothermal aureoles. *European Journal of Mineralogy* 11, 253–262. <https://doi.org/10.1127/ejm/11/2/0253>
- Maner, J.L., London, D., Icenhower, J.P. (2019) Enrichment of manganese to spessartine saturation in granite pegmatite systems. *American Mineralogist* 104, 1625–1637. <https://doi.org/10.2138/am-2019-6938>
- Mikova, J., Novák, M., Janousek, V. (2010) Boron isotopes in tourmalines of dravite–schorl series from granitic pegmatites of the Moldanubicum Zone, Czech Republic. *Acta Mineralogica-Petrographica Abstract Series* 6, 475.
- Ribeiro da Costa, I., Mourão, C., Récio, C., Guimarães, F., Antunes, I.M., Ramos, J.F., Barriga, F.J.A.S., Palmer, M.R., Milton, J.A. (2014) Tourmaline occurrences within the Penamacor-Monsanto granitic pluton and host-rocks (Central Portugal): genetic implications of crystal-chemical and isotopic features. *Contributions to Mineralogy and*



- Petrology* 167, 1–23. <https://doi.org/10.1007/s00410-014-0993-7>
- Siegel, K., Wagner, T., Trumbull, R.B., Jonsson, E., Matalin, G., Wälle, M., Heinrich, C.A. (2016) Stable isotope (B, H, O) and mineral-chemistry constraints on the magmatic to hydrothermal evolution of the Varuträsk rare-element pegmatite (Northern Sweden). *Chemical Geology* 421, 1–16. <https://doi.org/10.1016/j.chemgeo.2015.11.025>
- Trumbull, R.B., Beurlen, H., Wiedenbeck, M., Soares, D.R. (2013) The diversity of B-isotope variations in tourmaline from rare-element pegmatites in the Borborema Province of Brazil. *Chemical Geology* 352, 47–62. <https://doi.org/10.1016/j.chemgeo.2013.05.021>
- Trumbull, R.B., Krienitz, M.-S., Grundmann, G., Wiedenbeck, M. (2009) Tourmaline geochemistry and  $\delta^{11}\text{B}$  variations as a guide to fluid–rock interaction in the Habachtal emerald deposit, Tauern Window, Austria. *Contributions to Mineralogy and Petrology* 157, 411–427. <https://doi.org/10.1007/s00410-008-0342-9>
- van Hinsberg, V.J., Marschall, H. (2007) Boron isotope and light element sector zoning in tourmaline: Implications for the formation of B-isotopic signatures. *Chemical Geology* 238, 141–148. <https://doi.org/10.1016/j.chemgeo.2006.11.002>
- van Hinsberg, V.J., Schumacher, J.C. (2007) Intersector element partitioning in tourmaline: a potentially powerful single crystal thermometer. *Contributions to Mineralogy and Petrology* 153, 289–301. <https://doi.org/10.1007/s00410-006-0147-7>
- van Hinsberg, V.J., Schumacher, J.C., Kearns, S., Mason, P.R., Franz, G. (2006) Hourglass sector zoning in metamorphic tourmaline and resultant major and trace-element fractionation. *American Mineralogist* 91, 717–728. <https://doi.org/10.2138/am.2006.1920>
- Wolf, M.B., London, D. (1997) Boron in granitic magmas: stability of tourmaline in equilibrium with biotite and cordierite. *Contributions to Mineralogy and Petrology* 130, 12–30. <https://doi.org/10.1007/s004100050346>
- Zhao, H.D., Zhao, K.D., Palmer, M.R., Jiang, S.Y. (2019) In-situ elemental and boron isotopic variations of tourmaline from the Sanfang granite, South China: Insights into magmatic-hydrothermal evolution. *Chemical Geology* 504, 190–204. <https://doi.org/10.1016/j.chemgeo.2018.11.013>
- Zhao, K., Zhang, L., Palmer, M.R., Jiang, S., Xu, C., Zhao, H., Chen, W. (2021) Chemical and boron isotopic compositions of tourmaline at the Dachang Sn-polymetallic ore district in South China: Constraints on the origin and evolution of hydrothermal fluids. *Mineralium Deposita* 56, 1589–1608. <https://doi.org/10.1007/s00126-021-01045-4>

